TOPICAL REVIEW • OPEN ACCESS

A review of imaging methods for detection of photoluminescence in field-installed photovoltaic modules

To cite this article: M Vuković *et al* 2024 *Prog. Energy* **6** 032001

View the article online for updates and enhancements.

You may also like

- Structural study of single Shockley stacking faults terminated near substrate/epilayer interface in 4H-SiC
Johji Nishio, Chiharu Ota and Ryosuke Iijima
- Detection of finger interruptions in silicon solar cells using photoluminescence imaging
Lei Zhang, , Peng Liang et al.
- Outdoor luminescence imaging of field-deployed PV modules
Oliver Kunz, Jan Schlipf, Andreas Fladung et al.

This content was downloaded from IP address 128.39.70.127 on 21/05/2024 at 08:22

IOP Publishing Prog. Energy 6 (2024) 032001 https://doi.org/10.1088/2516-1083/ad4250

Progress in Energy

TOPICAL REVIEW

A review of imaging methods for detection of photoluminescence in field-installed photovoltaic modules

M Vuković[1,*], M S Wiig[1], G A dos Reis Benatto[2], E Olsen[3] and I Burud[3]

[1] Department for Solar Power Systems, Institute for Energy Technology, Kjeller, Norway
[2] Department of Electrical and Photonics Engineering, Technical University of Denmark, Roskilde, Denmark
[3] Faculty of Science and Technology, Norwegian University of Life Sciences, Ås, Norway
[*] Author to whom any correspondence should be addressed.

E-mail: marija.vukovic@ife.no

Keywords: photoluminescence, review, imaging, field-installed, photovoltaic, fault detection

OPEN ACCESS

RECEIVED
7 November 2023

REVISED
28 February 2024

ACCEPTED FOR PUBLICATION
23 April 2024

PUBLISHED
7 May 2024

Original Content from this work may be used under the terms of the Creative Commons Attribution 4.0 licence.

Any further distribution of this work must maintain attribution to the author(s) and the title of the work, journal citation and DOI.

Abstract

Contactless detection with a camera of radiation emitted from silicon solar cells resulting from band-to-band recombination after charge carrier excitation with an illumination source, i.e. photoluminescence (PL) imaging, has shown a great potential in the laboratory setting. In the recent years, the first approaches to PL imaging in the outdoor setting have been conducted on silicon modules with the Sun, a LED module and laser as excitation sources. The reason for these attempts has been that fault detection in photovoltaic (PV) modules using imaging can be more efficient and accurate than fault detection using electrical parameters. Developments in fault detection and localization are necessary because accurate monitoring of solar plants is expected to be one of the critical tasks facing the energy industry, when one considers that PV energy conversion will be the largest installed power capacity by 2027 and that the utility-scale solar PV electricity generation will be the least costly option for new electricity generation in many of the world's countries. The present study sums up the different methods for outdoor PL imaging and emphasizes their differences regarding filtering of the reflected excitation light from the PL signal. The different types of PL images obtained from each method and the image processing algorithms are described. Finally, the interpretation of the different types of PL images is addressed.

1. Introduction

Year 2022 was the year when the global installation of solar energy production reached 1 TW, with increasingly ambitious targets being set [1]. Compared to other renewable energy sources, solar photovoltaic (PV) accounts for more than 60% of all renewable capacity expansion. The International Energy Agency predicts that PV energy conversion will be the largest installed power capacity worldwide by 2027, totaling more than 2.35 TW. For a significant majority of the world's countries, utility-scale solar PV is the least costly option for new electricity generation [2]. However, ensuring efficient and accurate monitoring of solar plants for localizing and detecting faults is one of the main critical tasks facing the energy industry [3–5].

Two main groups of inspection techniques for PV power plants have been proposed thus far. The first group is based on measurements of electrical parameters [3], in which a common way of monitoring solar plants is with different types of current and voltage sensors [4]. They are usually attached to an array or a string, and their mounting is intrusive. Measurements can also be conducted at the module level, but this requires identifying, locating and disassembling a faulty module. This is time-consuming and costly [4, 6]. In addition, the exact location of the fault is not provided, as current and voltage sensors have a limited ability to pinpoint the cause of the power loss [3, 7, 8]. The second group is based on measurements of emitted or reflected radiation with cameras. This type of inspection enables a higher level of granularity and contactless inspection at the module level and can be combined with unmanned aerial vehicles (UAVs) for fast detection and localization of faults [3–5].

© 2024 The Author(s). Published by IOP Publishing Ltd

Camera-based inspection methods can be characterized as contactless because the camera sensor does not require any contact with the PV system. However, although no camera requires contact with the PV system, there are some camera-based inspection techniques that require contact to produce the radiation that is being detected, such as in the case of luminescence-based imaging. No type of interference with the PV system is required in case of imaging in the infrared range with a thermal infrared (TIR) camera and in the visible light range with an RGB camera [5].

Inspection with a TIR camera is the most common inspection technique in combination with a UAV. The underlying principle is that many of the defects in a PV module generate heat under sunlight and therefore under operation. These defects are visible in TIR images as increased temperature compared to a healthy cell. However, it is not possible to distinguish different defects, such as cracked cells, mismatched cells or partially disconnected ribbon, based on heat generation. Therefore, it is often not possible to identify the exact origin of the defect based on a TIR image alone. In addition, cases of cracked cells and electrically isolated regions have been observed, which are not visible as increased temperature on TIR images [5, 8, 9].

An RGB camera detects reflected sunlight in the visible range. This camera can provide higher resolution than a TIR camera, and in that way, help identify the reason for defects detected on TIR images. This has been done in combination with a UAV inspection. However, the signal that the RGB camera detects enables identification of only those faults observable by the human eye [5, 6, 10].

In addition to reflected sunlight in the visible range, RGB cameras can detect emitted radiation (fluorescence) from fluorophores upon excitation with ultraviolet (UV) light. Fluorophores are chemical compounds in polymeric lamination material in PV modules and are prone to degradation due to reaction with oxygen, in which case their fluorescence emission is weakened and is thus depicted with lower pixel values in images. In combination with imaging from UAVs, ultraviolet fluorescence (UVF) imaging poses some challenges [11]. The UAV needs to carry the UV illumination source and the accompanying battery. At high flight altitudes, UV light and correspondingly the emitted fluorescence signal are very weak [9], while low altitudes have a negative effect on throughput. UVF imaging requires long exposure times due to the relatively low intensity of the emitted radiation, but low exposure times are favorable due to the vibration and moving of the UAVs. The inspection must be conducted in the dark due to the strong reflected sunlight in the visible range [5, 11].

The electroluminescence (EL) imaging technique is based on detecting radiative band-to-band recombination in the semiconductor material emitted upon excitation with forward current bias. Areas with defects emit weaker radiation compared to healthy areas and therefore have lower pixel values. EL images have a greater level of detail and information than that can be obtained from the above-mentioned imaging techniques [5, 8].

EL imaging outdoors has traditionally been conducted in the dark or in very low light conditions, so that daylight does not interfere with the EL signal detection. In such conditions, EL imaging has been combined with UAVs. However, the disadvantage of night flying is that the UAV control is more difficult and risky at the same time as it is more regulated and requires more training. Furthermore, an EL inspection requires connection of the strings to a DC power supply, which again results in a more complicated movement across the plant in the night [12]. This makes the UAV inspection less efficient and requires electrician on site [9]. Other operational and safety issues have to do with potentially harsher environmental conditions during nighttime [12]. Daylight imaging procedures have also been developed in recent years [5, 13].

An alternative to EL imaging is photoluminescence (PL) imaging. PL imaging is based on charge carrier excitation through photons, that is, an illumination source. As the information obtained from such images is comparable to that from EL images, it can be employed as their alternative [5, 9]. The development of PL imaging approaches in the outdoor setting started only a few years ago. Nevertheless, PL imaging has been categorized as an inspection technique for PV module degradation in the field [14] and as an imaging technique for monitoring of large-scale PV power plants [6]. In these two cases, PL imaging is presented in the context of other imaging techniques. PL imaging has been discussed in a technical report as one of several on-site inspection techniques for qualification of PV power plants, in which a thorough description of two PL imaging approaches has been presented [9]. A recent review of outdoor luminescence imaging of field-deployed PV modules focuses solely on EL and PL imaging methods, in which some daylight PL imaging methods and their readiness for commercial use are discussed [8].

The present study focuses solely on the PL imaging methods. It gives a comprehensive overview of the approaches to PL imaging for daytime and nighttime imaging based on the equipment needed for their realization. It also presents two important aspects of PL imaging which deserve special attention. One is the different types of images which result from the different methods and processing algorithms. Five types of PL images result from the different imaging methods and four types of final images resulting from the different processing algorithms. The second important aspect is their interpretation depending on imaging method and/or algorithm applied. This work is organized as follows. After a brief description of the principle behind

PL signal emission in section 2, section 3 gives a detailed account of approaches for PL signal detection at nighttime and daytime. section 4 explains what types of PL images result from the presented imaging methods and how they can be processed, before section 5 addresses the issue of their interpretation. Finally, an overview of all the mentioned studies and their main aspects is summed in a table in section 6.

2. PL emission from silicon material

Radiative band-to-band recombination in silicon (Si) material originates from the de-excitation of charge carriers from the conduction band to the valence band. A photon, whose energy corresponds to the band gap energy of Si, is emitted upon recombination. The signal emitted from the Si material upon de-excitation is called PL if the excitation before it takes place with photons (i.e. an illumination source). The intensity of PL I_{PL} can be expressed as

$$I_{\mathrm{PL}} = C n_i^2 \exp\left(\frac{eV_d}{kT}\right), \tag{1}$$

where C is a proportionality factor that accounts for the optical properties of the sample, n_i is the intrinsic carrier density, e is the elementary charge, V_d is the diode voltage, k is the Boltzmann constant and T is the temperature [5, 15].

The two conditions for emission of the minimum and maximum intensity of the PL signal are illustrated in the current–voltage (IV) characteristics in figure 1. As the intensity of the signal is proportional to the exponential of the diode voltage, the highest signal intensity is achieved in the open-circuit (OC) condition in which there is no current extraction. The lowest signal intensity can be measured in the short-circuit (SC) condition, when the current extraction is at its maximum. Thus, unless one needs to extract current during PL signal detection, this type of imaging is performed in the OC condition, without any contact with the sample, on both Si bricks, as-cut wafers and solar cells [5, 15].

3. PL detection

The PL signal from crystalline Si peaks at around 1140 nm [15]. Its detection can be performed with a light source, which illuminates the material and excites the charge carriers, and a camera or a spectrometer, which detects the emitted luminescence. A camera provides the spatial resolution of the signal as opposed to the point measurement obtained with a spectrometer [5]. Camera detectors used for PL imaging are either silicon (Si) or indium gallium arsenide (InGaAs) detectors. For imaging outdoor, InGaAs cameras are preferred [16–23] because of their high quantum efficiency in the relevant wavelength region [8].

Depending on the wavelength range of the camera detector and the excitation source, the camera might detect the reflected light from the excitation source in addition to the PL signal. In a controlled laboratory setting, the experiment is designed in such a way that the reflected light and the emitted PL signal do not overlap spectrally. In this case, it is possible to filter out the former with optical filters [5, 24]. The approach for filtering of reflected light from the excitation source when working outdoor depends on whether the imaging is conducted at nighttime or daytime.

3.1. Outdoor PL detection at nighttime

In case of outdoor PL imaging at night, the same approach to filtering can be applied as in case of imaging in a laboratory setting. There is relatively little pollution from other light sources in a dark environment and one can use optical filters in combination with artificial illumination sources. A PL imaging method developed for nighttime imaging has been proposed with a set-up consisting of white LED modules used as illumination source. Their excitation wavelength is in the visible spectrum, which means that the photons have enough energy to excite an electron in Si material. Two types of filters are used. A short-pass filter on each LED module transmits the emission of light below 800 nm and a long-pass filter on the camera side transmits the light above 970 nm. This is illustrated in figure 2, which is based on explanations provided in [16, 17, 25]. The short-pass filter on the LED modules ensures that the light with wavelengths above 800 nm does not reach the cells, at the same time as the long-pass filter on the camera ensures that only light above 970 nm reaches the camera detector. The region between 800 nm and 970 nm is blocked by both filters [16, 17, 26].

The LED modules are assembled to allow illumination of one module at a time [16, 17, 26]. The challenging aspect of using an artificial illumination source to illuminate an area as large as a whole module is the homogeneity of illumination. The intensity of illumination affects the intensity of PL emission and therefore the appearance of cells and their defects. This is particularly the case when using a fewer number of LED modules due to weight issues, four instead of eighteen, in case of aerial imaging with a drone [16, 17]. Furthermore, the LED modules require powering, which also needs to be taken into account.

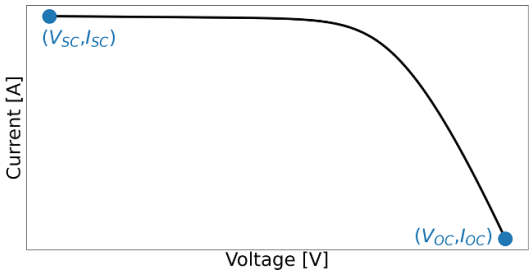

Figure 1. IV curve illustrated with the two points in which the intensity of the PL signal is at its minimum, the SC condition, and at its maximum, the OC condition. Reproduced with permission from [5]. CC BY-NC-ND 4.0.

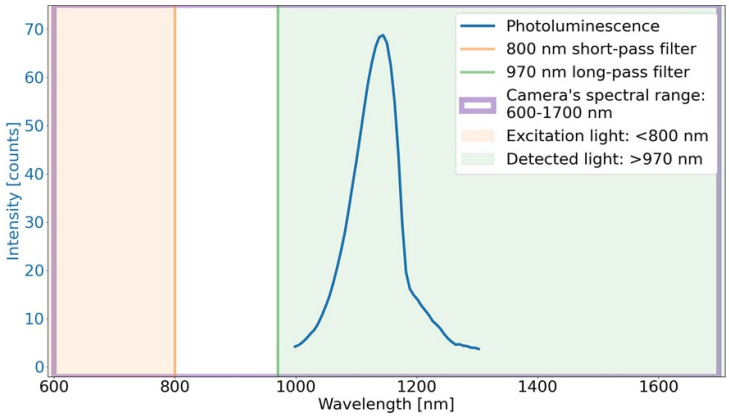

Figure 2. Illustration of relevant wavelength ranges for nighttime PL imaging under LED module excitation. The spectral range of the camera is given in purple [25]. The short-pass filter on the LEDs blocks the excitation light above 800 nm, while the long-pass filter on the camera blocks the reflected light below 970 nm [16, 17]. In that way, only the emitted PL signal is detected.

The advantage of this method for PL image acquisition is that it does not require any contact with the PV system for image acquisition, as is the case for many daylight PL imaging techniques. This will be elaborated in the following section. Because the reflected light from the excitation source is blocked with filters, no image processing is required to eliminate the reflected signal from the images. This means that these PL images contain the absolute PL signal and not the difference PL signal, ΔPL, as is the case with methods described below.

A proof-of-concept of a similar approach has been developed with what seems to be a collection of red LEDs on a movable bed. It slides from module to module and illuminates them, while a camera acquires images. The device is called *PLatypus* [27].

Another imaging method proposed for low light conditions in the surroundings is illumination with laser light. An 808 nm line laser attached to a rotated robot arm was used as an excitation source. It scanned the region of interest consisting of four cells from two directions, perpendicular and parallel orientation with respect to the busbars. This resulted in two images. An InGaAs camera was used with a 950 nm long-pass filter which lets through only the PL signal above 950 nm and blocks the reflected laser light below 950 nm [28]. The challenge with this imaging method is, as mentioned above in case of LED modules, that the intensity of the excitation light might be inhomogeneous [29]. One also needs to control the scanning process with the laser.

3.2. Outdoor PL detection at daytime

When imaging field-deployed modules in daylight, the spectral range of the reflected sunlight and the emitted PL signal overlap. This is illustrated in figure 3. Although the solar irradiance in the wavelength range in which the PL signal is emitted is weakened when it reaches the Earth's surface due to water absorption in the atmosphere, the irradiance is still orders of magnitude stronger when reflected from the modules compared to the PL signal [5].

The challenge regarding the separation of two spectrally overlapping signals is translated to average pixel values, as illustrated in figure 4. The camera detector registers the total signal, which is the sum of the reflected sunlight and the emitted PL signal. If a camera is placed in front of a module in operation under constant irradiance, that is, in clear sky conditions, and a series of images is acquired, the PL signal and

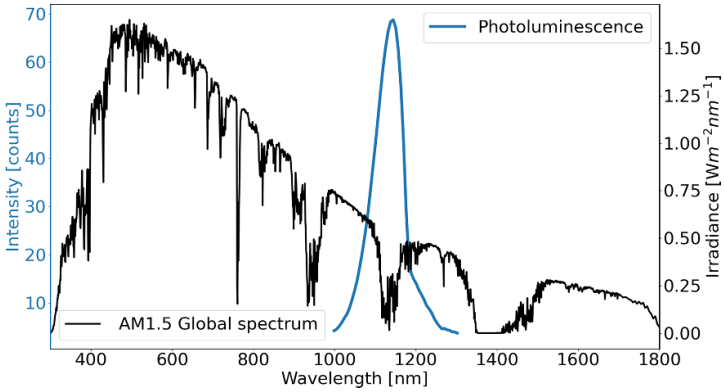

Figure 3. The AM1.5 global spectrum [30] overlaid with the PL signal detected from a Si solar cell in a controlled laboratory environment with laser light excitation and a hyperspectral camera. Reproduced with permission from [5]. CC BY-NC-ND 4.0.

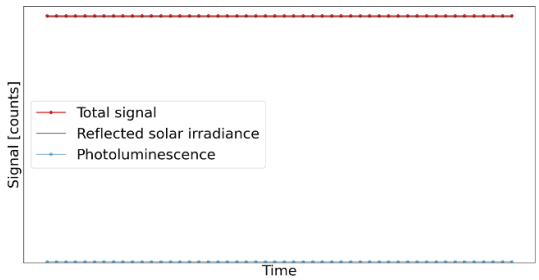

Figure 4. Signal intensity from PV modules detected with a series of images during constant illumination is translated into the average pixel count over time. It shows the total signal detected and its constituent parts, the reflected sunlight and the PL signal. Reproduced with permission from [5]. CC BY-NC-ND 4.0.

reflected solar irradiance are two constant signals detected over time. The PL signal is almost nonexistent compared to the high intensity of the reflected solar irradiance. The total signal is shifted upwards only slightly from the reflected solar irradiance signal due to the PL emission. Based on this image series, it is not possible to know what proportion of a pixel value is due to the reflected solar irradiance or the PL signal [5].

Different solutions have been proposed for elimination of the reflection and extraction of the emitted signal due to the spectral overlap of the wavelength range in which the PL signal is emitted, and the light from the excitation source is reflected. The methods can be divided into two groups: manipulating the PV system, which can again be divided into explicit control of the PV system's operating point (OP) [12, 18–20, 31–35] and imaging during IV curve sweeps [21, 22, 36], and filtering through optical filters [37, 38]. The following section elaborates on these approaches [5].

3.2.1. Control of the OP

The PL signal can be separated from the total signal if it varies in a controlled way while the reflected solar irradiance remains constant. This is the essence of the lock-in technique. The technique is used for signal amplification and evaluation against a noisy background and is based on periodically pulsed amplitude modulation of the primary signal with a particular frequency [32, 39]. This is illustrated in figure 5. The primary signal is the PL signal, which is modulated between low and high amplitudes, PL_1 and PL_2. The background signal is the reflected sunlight, R, assumed to be constant between the two modulation conditions [5].

Four repetitions of the two modulation states are depicted in figure 5, during which eight images can be acquired. The total signal detected in each image is shown in figure 6 as the average pixel count over time. Compared to figure 4, the PL signal in figure 6 varies in intensity up and down from image to image. The variation of the PL signal between two levels makes it possible to identify how much of the total signal is the PL signal in the high state, PL_2, compared to the low state, PL_1 [5]. How the PL signal can be extracted from these images will be elaborated on in the section on image processing.

Because the intensity of the PL signal is proportional to the exponential of the diode voltage, according to equation (1), the intensity of the PL signal can be controlled between a high and a low state by controlling the OP of the imaged modules. Control of the OP along the IV curve can be achieved with electrical or

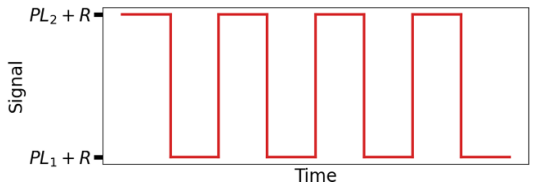

Figure 5. The total signal consisting of the PL signal and reflected sunlight, *R*, can be detected over time with high and low intensity due to pulsed amplitude modulation of the PL emission from PV modules. The PL signal has high intensity, PL_2, and low intensity, PL_1. Reflected sunlight, *R*, is assumed to be constant. Reproduced with permission from [5]. CC BY-NC-ND 4.0.

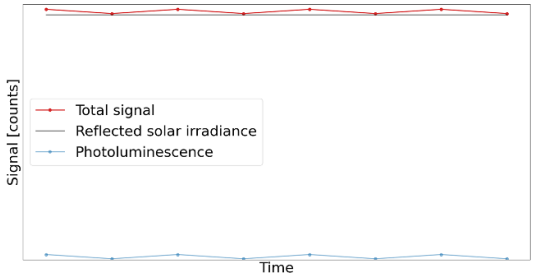

Figure 6. The PL signal, reflected solar irradiance and the total signal detected in each image during lock-in modulation. Reproduced with permission from [5]. CC BY-NC-ND 4.0.

optical modulation. The assumption of constant reflected solar irradiance during imaging requires a fast, almost instantaneous, switching of the OP. Frequencies of 25 Hz and 30 Hz have been reported [5, 18, 34].

Several solutions have been proposed that use electrical modulation of the OP. The first developed daylight luminescence imaging procedure is based on a patented DaySy imaging system consisting of a DaySyBox and the imaging apparatus [32]. The box can be connected to up to six strings or a power source to modulate the system between the SC, maximum power point (MPP), OC and forward current bias. It is possible to conduct EL imaging in daylight and at night as well as daylight PL imaging [5, 9, 31, 33].

The lock-in technique with electrical modulation can be implemented in other ways as well. The OP of one module can be controlled with a modulator that uses a metal-oxide-semiconductor field-effect transistor (MOSFET) as a switch. A programmable DC load in combination with a MOSFET makes it possible to choose the OPs on the IV curve more freely [34]. Another study uses a solid-state relay for switching a module between the OC and SC conditions [12]. At the string level, one can apply manual switching of one or several strings through a combiner box. In this way, the OP of the string can be switched between the MPP and the OC [5, 35].

Optical modulation has been proposed to avoid interfering with the electrical connections of the modules or strings [18, 20]. Optical modulation is based on controlling the OP of a sub-string in a module by covering one of its cells with an LED. By doing so, the amount of shading on that one cell, and thus the extracted current for all the cells in the sub-string connected in series to the same bypass diode, is controlled [5, 18, 20]. The prerequisite for this approach is for the module to be in operation, meaning that it cannot be in the OC condition. If that were the case, covering of one cell in a sub-string would not lead to any variation in extracted current, which is what is achieved with this approach.

In the normal field operation, the switching can be performed between the OC condition and any OP between the OC and MPP. In the proof of concept study [18], the switching was performed between the OC condition by completely shading one cell (0 Sun), in which case the bypass diode leads, and the SC condition by illuminating it with 1 Sun. The imaging was conducted at the sub-string level and by moving the LED from one sub-string to the next. The images are then stitched into an image of a whole module [5, 18].

This approach has been tested for PV systems having module level power electronics, an example of which is a module connected to a microinverter. In this case, it is possible to switch the OP of the entire module by controlling the current through one cell. It was investigated how power electronics affects the almost instantaneous switching. It is found that the particular inverter has a reaction time of 6 s when switched from the OC condition to the MPP condition. Because of the changes in irradiance that could take place during this switching time, the sequential switching method, as illustrated in figure 5, is not applicable, and the batch measurement approach was proposed [19]. This approach is illustrated in figure 7. During each of the two states of PV module emission, an image series is acquired. The OP is switched at time t_1, and

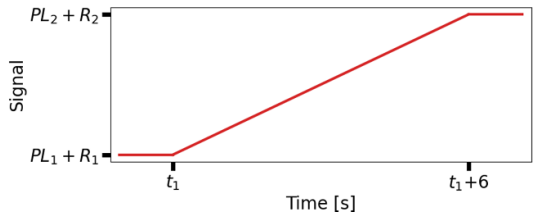

Figure 7. The total signal consisting of the PL signal and reflected sunlight as a function of time when the lock-in technique is performed on a PV module connected to a microinverter. The inverter has a reaction time of approximately 6 s [19]. The reflected solar irradiance can no longer be assumed to be constant and is called R_1 and R_2. The shape of the line between the two states does not illustrate the level of the total signal during the inverter's reaction time but the length of the time compared to instantaneous switching in figure 5. Reproduced with permission from [5]. CC BY-NC-ND 4.0.

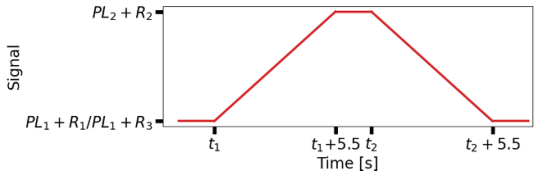

Figure 8. Modified approach to image acquisition from figure 7. The reaction time of the string inverter was measured to 5.5 s. Three sets of images are acquired in states MPP, OC and MPP. Reproduced with permission from [5]. CC BY-NC-ND 4.0.

the new operating condition is reached at $t_1 + 6$. As the irradiance might change in the meantime, it is no longer assumed to be constant and is called R_1 and R_2 in figure 7. A correction due to the changing reflected solar irradiance was proposed [5, 19].

The approach with optical modulation was extended to enable a higher throughput by developing an optical modulator consisting of several LEDs. The modulator can cover the necessary number of cells in several modules to switch the OP at the string level. The proposed method controls the OP of five modules in a string of 28 modules. One of the assumptions is that the modules are typically series connected in strings of 27–29 modules. Forcing five modules in the OC condition will cause the remaining 23 modules to compensate for this voltage loss by increasing their voltages because the string voltage is fixed by the PV plant design. The increase in voltage by the remaining modules will be around 18%, which is enough to force also these modules in the OC condition and thus increase the PL signal emission in the whole string. Another underlying assumption is that a PV array may consist of 200 or more module strings connected in parallel. Modulating one such string will affect the array current by less than 0.5% and thus will not cause the inverter's OP to change significantly [5, 20]. The challenge for high throughput with this method is that the optical modulator needs to be moved from string to string.

An example of electrical modulation on string level was developed based on the idea of modulation while a module is connected to a microinverter, mentioned above. The modulation of the OP is obtained directly through the string inverter by establishing communication with it through communication protocol Modbus TCP. This method can be carried out remotely over a WiFi connection. In this way, it is possible to modulate the OPs of several strings simultaneously without physically connecting to the strings. The approach can modulate the OP along the IV curve between the MPP and OC conditions. Due to the string inverter's reaction time of 5.5 s, image acquisition with delayed modulation, according to figure 7, was used as a starting point. However, a 5.5 s delay had a negative effect on image quality and it was therefore necessary to acquire more images during one more switch from OC back to MPP condition, as illustrated in figure 8. In that way three series of images were acquired instead of two, as shown in figure 7. However, the method is still unstable. The reason for that might be that it was tested on aluminum back-surface field (Al-BSF) cell technology. Imaging modules with higher open circuit voltage V_{OC} might give better results [5, 23].

Although the approaches for electrical and optical modulation described thus far are employed to enable filtering of the reflected sunlight during image processing step, the camera apparatus also needs to be used in combination with an optical band-pass filter. Such a filter is used to decrease the intensity of the reflected sunlight, which is being detected. The studies described thus far use a short-wave infrared camera with an InGaAs detector. The spectral range of one such camera, Raptor Photonics Owl 640S, is usually 900–1700 nm. The band-pass filter mounted on it transmits the range of 1125–1175 nm and has a center wavelength (CWL) at 1150 nm [23]. Omitting optical filters would result in the detection of the reflected sunlight in the wide spectral range of the camera. This would result in saturation of the total detected signal during imaging in

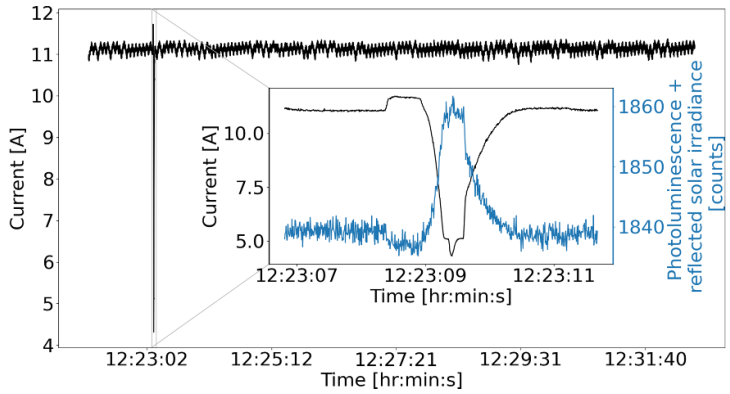

Figure 9. Current measured over time shows a string in MPP before a sudden drop in current takes place due to an IV curve sweep. The zoomed region shows the change in current and in the total detected signal, reflected solar irradiance and PL.

bright daylight. Band-pass filters are used in combination with electrical and optical modulation to narrow down the spectral range of interest and therefore the amount of detected reflected sunlight [5].

3.2.2. IV curve sweep

The change in the PL signal as a way of filtering out the reflected solar irradiance can be detected without controlling the OP of the PV system. String inverters nowadays are equipped with the functionality to conduct IV curve sweeps, which means that the PV system undergoes a wide range of OP from the SC to close to OC condition (figure 1). Consequently, the emission of PL signal follows this change and therefore a continuously changing PL signal can be detected [21].

This functionality is implemented in string inverters in different ways. A string inverter of type Fronius Primo 3.0 initiates IV curve sweeps on its own every 10 min for a global MPP search as part of its intelligent shade management system [21, 40]. Other types of inverters can conduct IV curve sweeps on command through a smartphone application for monitoring purposes. They can be initiated by the string inverter or by an operator and conducted at the plant, array or string level depending on the particular solution [5, 22, 40–43].

The approach developed for PL imaging during IV curve sweeps was conditioned by the fact that the string inverter in question could not be controlled with respect to when it conducts IV curve sweeps [21]. The camera was placed in front of a module string and it started to collect images. Current measurements were collected simultaneously for better insight into when an IV curve sweep would take place [5]. The sudden IV curve sweep is shown on current measurements in figure 9. The zoomed in region of the IV curve sweep overlaid with the average pixel count from the images shows how the signal changes on average throughout an image series. The values on the x-axis show that close to 200 000 images were acquired while waiting for the IV curve sweep to take place. This approach needs to be made more efficient by enabling unsupervised image processing in real time based on which the occurrence of the IV curve sweep would be detected [21, 22].

The advantage of this approach is that it does not require interference with the production in the same way as the lock-in technique. It is not necessary to connect to the modules with an additional piece of equipment, which might be dimensioned for only a certain number of modules. Additionally, the acquired signal covers a wide range of OPs, resulting in several interpretable images, as will be discussed in section 4. The disadvantage is that a string inverter might not be controllable with respect to when it conducts the IV curve sweep, and therefore one might need to wait for it to take place [21, 22, 36].

3.2.3. Optical filtering

Two approaches to optical filtering have been proposed thus far. The approaches do not require connection to the PV system to separate the reflected sunlight from the PL signal.

The first approach is described in figure 10. Two images are acquired. One image is acquired with a band-pass filter with a CWL where the PL signal peaks at around 1135 nm. This is also the spectral region in which the water vapor absorbs. In this way, the ratio between the emitted PL and the reflected sunlight is maximized. The other image is acquired with a band-pass filter in the spectral region where the PL signal is weak, either around 1050 nm or 1200 nm. These two filters are chosen so that almost no PL signal is detected in their spectral ranges at the same time as the ambient reflected signal is similar to that detected with the first filter. A difference image is obtained between the image with high PL signal intensity and one of the

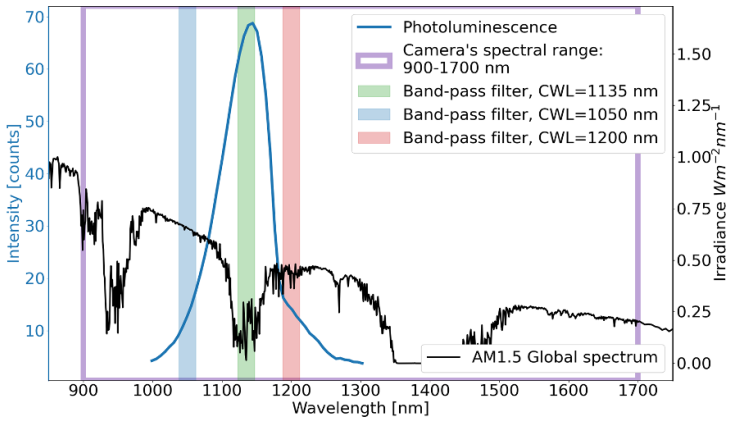

Figure 10. The AM1.5 global spectrum [30] and the PL signal are shown in the spectral range of 850–1750 nm. The green, blue and red squares indicate the spectral range of three band-pass filters with their CWLs as used in [5, 37]. Reproduced with permission from [5]. CC BY-NC-ND 4.0.

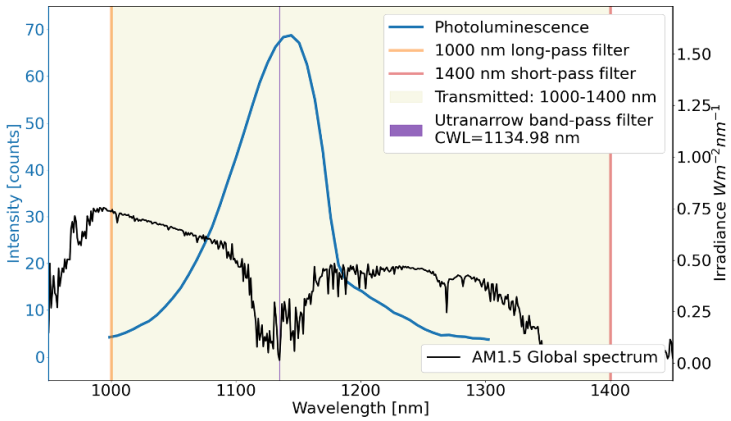

Figure 11. The AM1.5 global spectrum [30] and the PL signal are shown in the spectral range of 950–1450 nm. The yellow square indicates the spectral range (1000–1400 nm) in which the signal passes through the filter system based on the combination of a long-pass and a short-pass filter. The thin purple line indicates the spectral range in which the ultranarrow band-pass filter transmits [5, 38]. Reproduced with permission from [5]. CC BY-NC-ND 4.0.

images with low signal intensity [5, 37]. It is argued that a difference image obtained with the image acquired at the 1200 nm region gives better results due to smaller change of the reflected solar irradiance in that part of the spectrum than in the region around 1050 nm [37].

The imaging was performed in the OC condition, but it should be possible to perform it during regular operation of field-deployed modules in the MPP condition. The challenge in that case will be that the PL signal will be up to 20 times weaker. The method is particularly suitable for high-efficiency modules because they have a relatively high ratio of the PL signal to the reflected sunlight [5, 37].

The other approach for PL imaging, which uses optical filtering, is based on ultranarrow band-pass filters [38]. In the spectral range 1134.5–1135.3 nm, the water vapor absorption in the atmosphere is so strong that almost none of the Sun's radiation reaches the Earth. The ultranarrow band-pass filters cover a bandwidth of 0.34 nm, with the CWL at 1134.98 nm. Almost no reflected sunlight is detected through such filters. This approach is illustrated in figure 11. In addition to the ultranarrow band-pass filter, a long-pass and a short-pass filter are used to further reduce the unwanted reflected solar irradiance being detected below 1000 nm and above 1400 nm [5].

Several interesting PL imaging aspects originate from this imaging method. The PL signal intensity has been found to decrease with increasing distance due to its absorption by water vapor on its way from the module to the camera detector. The optical absorption length in the spectral range is 12 m [8, 38]. Depending on the application, this method requires long acquisition times. To obtain high-quality images displaying micro-cracks in the OC condition, an acquisition time of 20 s and 50 s was used with a heterojunction module ($V_{OC} = 735$ mV cell^{-1}) and a passivated emitter and rear contact solar cell (PERC) module ($V_{OC} = 686$ mV cell^{-1}), respectively. For reliable defect detection, an exposure time of 1 s can also be used

during imaging of PERC modules [38]. Moreover, regarding image quality, an area around the PL image edges is blurry because of the custom-designed imaging optics [8]. Concerning the investigation of series resistance-related defects, it is necessary to acquire PL images during current extraction. To do that, control of the OP is needed. The use of optical modulation with LEDs is proposed [38], as described above [5].

4. Types of PL images and processing algorithms

The approaches presented above can be visualized, as shown in figure 12. PL image acquisition can be conducted with a laser, LED modules or the Sun as the excitation source. The approach with laser uses an optical filter attached to the imaging apparatus in order to eliminate the reflected light from the excitation source. Imaging with LED modules uses the same approach in addition to filters attached to the illumination source. In case of imaging with Sun's excitation, filtering of reflected sunlight can be carried out with filters attached to imaging apparatus or by manipulating the PV system. The latter can again be divided into two approaches, explicit control of the OP and IV curve sweep. Controlling the OP can be carried out optically or electrically as well as instantaneously or in a delayed manner. The arrows in figure 12 represent the studies described in the two preceding sections.

The different approaches result in five types of acquired PL images. Imaging with laser excitation [28], LED modules excitation [16, 17] as well as under sunlight excitation using ultranarrow band-pass filters [38] results in PL images consisting only of the PL signal. The stippled orange lines indicate that the approach with ultranarrow band-pass filters can be combined with instantaneous control of the OP in order to acquire images under different level of current extraction. This will be elaborated in the following section. Imaging under sunlight excitation with two different filters on the camera apparatus [37] results in two types of acquired images in two different spectral regions. These consist of two different intensities of the PL signal and the reflected sunlight, $\mathrm{PL}_{S1}+R_{S1}$ and $\mathrm{PL}_{S2}+R_{S2}$. The instantaneous switching of the OP between two conditions results in images with two different PL signal intensities, but the reflected sunlight is expected to remain constant [8, 12, 18, 20, 31–34]. These images are termed $\mathrm{PL}_{\mathrm{OP1}}+R$ and $\mathrm{PL}_{\mathrm{OP2}}+R$. The delayed switching differs from instantaneous switching in the way that the reflected sunlight cannot be assumed constant and is termed R_1 and R_2 [19, 23, 35, 44]. The image acquisition during IV curve sweeps results in a series of N images during the change of the OPs of the PV system, $\mathrm{PL}_{\mathrm{OP}i}+R, i=1,2,\ldots,N$. No change in reflected sunlight was assumed for these data series [21, 22, 36].

The five types of raw sets of images can be processed in four different ways. The PL images obtained with no reflected light [16, 17, 38] do not require any processing. The images obtained with two different filters result in a difference PL image, $\Delta\mathrm{PL}_S$. It is obtained between two images acquired in two different spectral regions while the PV system is in the same OP. Acquisition of image pairs during modulation of the OP results in a $\Delta\mathrm{PL}_{\mathrm{OP}}$ image, which is a difference image obtained between two sets of images acquired in the same spectral region, but in different OPs. The image processing algorithm for instantaneous switching is shown in equation (2). A number of N image pairs is acquired interchangeably in two OPs, as illustrated in figure 6. Every image pair is subtracted and the average of differences is calculated. Since PL signal is weak, several pairs are averaged and the signal is enhanced in this way. In case of delayed modulation, the averaging needs to be conducted for each set of images obtained in each OP as indicated in figures 7, 8 and shown below in equation (3).

$$\Delta\mathrm{PL}_{\mathrm{OP}}=\frac{1}{N}\Sigma_{i=1}^{N}\left(PL_{2i}+R_i\right)-\left(PL_{1i}+R_i\right), \tag{2}$$

$$\Delta\mathrm{PL}_{\mathrm{OP}}=\frac{1}{N}\Sigma_{i=1}^{N}\left(PL_{2i}+R_{2i}\right)-\frac{1}{N}\Sigma_{i=1}^{N}\left(PL_{1i}+R_{1i}\right). \tag{3}$$

Processing of images acquired during IV curve sweeps was first conducted with equation (3). The relevant images for two image subsets were selected manually after image acquisition [21]. Because this approach does no result in immediate division of images into two groups as is the case with modulation between two OPs, manual selection of images poses challenges for fast image processing [22]. Another algorithm was proposed based on Pearson correlation coefficient (PCC), which results in $\mathrm{PCC}_{\mathrm{PL}}$ images, as shown below in equation (4). The correlation coefficient, ρ, is given as

$$\rho=\frac{\Sigma_{i=1}^{N}\left(X_i-\overline{X}\right)\left(Y_i-\overline{Y}\right)}{\sqrt{\Sigma_{i=1}^{N}\left(X_i-\overline{X}\right)^2}\sqrt{\Sigma_{i=1}^{N}\left(Y_i-\overline{Y}\right)^2}}, \tag{4}$$

where N is the number of data points (number of images), X is acquired signal in one pixel, Y is the reference signal, $\overline{X}$ and $\overline{Y}$ are their mean values. The reference signal is here defined as the average image pixel count

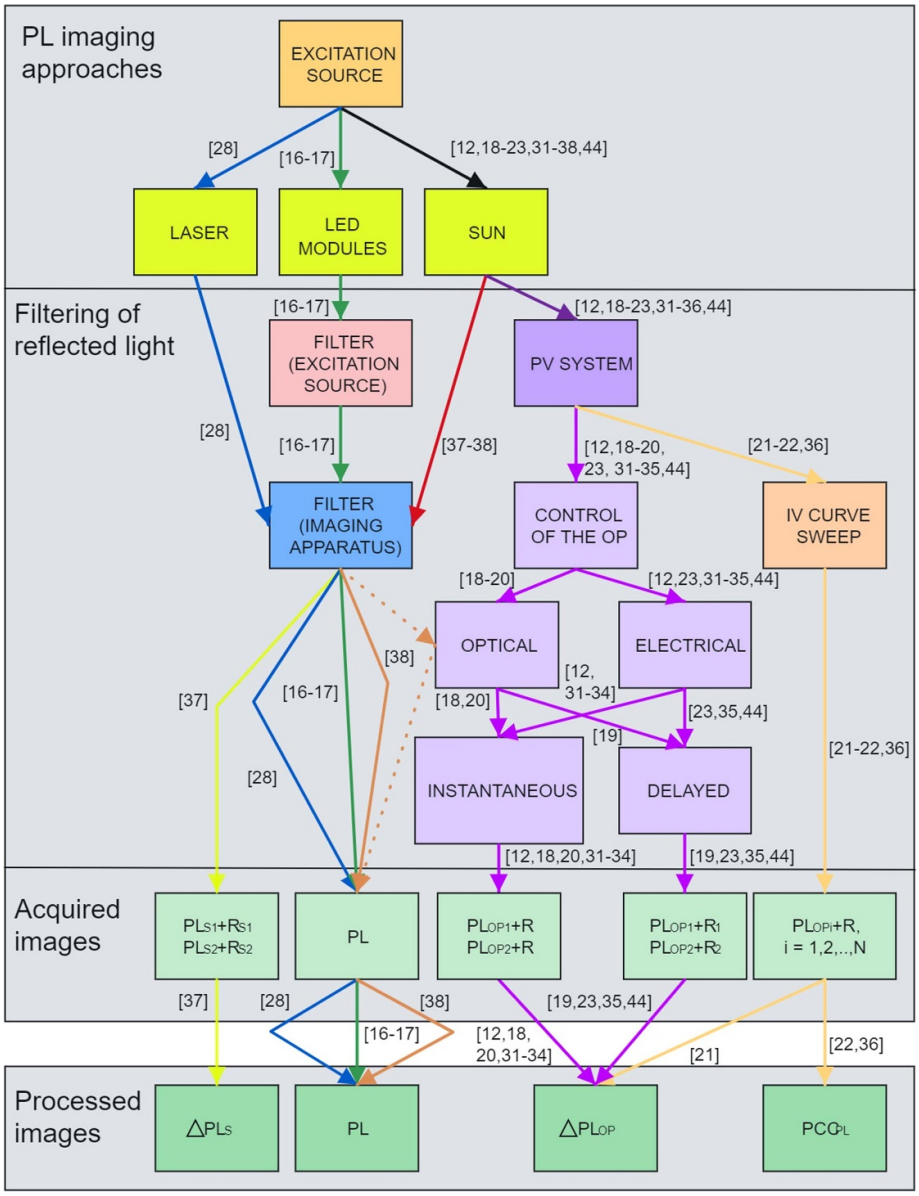

Figure 12. PL imaging under three different excitation sources, laser, LED modules and Sun, is shown with respect to solutions for elimination of reflected light. Five types of acquired images and four types of processed images are listed and ascribed to each imaging method. The studies are represented by the different arrow colors and referenced next to them.

over N images. It is dominated by the change in the PL signal, as shown in figure 9. The signal X in every pixel in the spatial domain is correlated with the reference signal. Those pixels whose signal resembles the reference signal will have high correlation (module pixels), while those pixels whose signal does not resemble the reference signal will have no correlation (background pixels). In this way the module pixels will be extracted from the background [22, 36].

5. Interpretation of PL images

The question arises which faults are visible and how they appear in the four types of processed images. It is important to emphasize that some faults are visible only if the resolution is sufficient. It has been reported that 1/5 of a module (2 × 6 cells [18] or 3 × 4 cells [31]) has been imaged for micro-cracks to be visible. In general, outdoor PL imaging is a fairly new approach for fault detection in field-installed PV modules. Information about what kinds of defects are visible in such images is still limited [5].

The study on PL imaging with two band-pass filters is a small study in which a ΔPL_S image of a few cells is displayed. The visible defects in ΔPL_S images are cracks [5, 37]. The PCC_{PL} images show very good correspondence with ΔPL_{OP} images. So far, it has been demonstrated that they show cracks and isolated regions [21, 22]. The studies in which ΔPL_{OP} images are obtained have shown that cracks and isolated

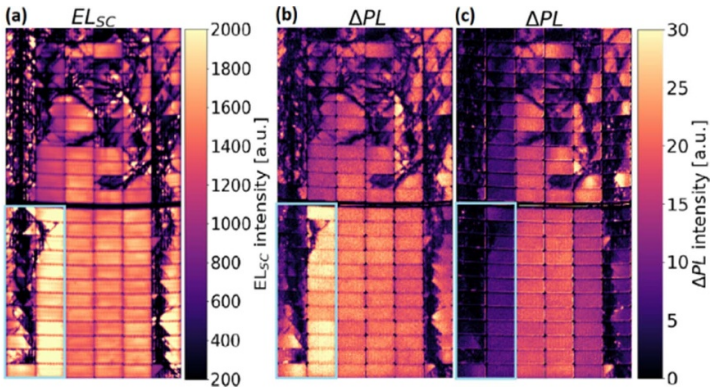

Figure 13. An EL_{SC} image (a) and two ΔPL_{OP} images (b)–(c). The ΔPL_{OP} were obtained from images acquired during different OPs of an IV curve sweep. Creative Commons CC BY license. Reproduced from [21]. CC BY 4.0.

regions [12, 18, 19, 31, 34, 35], bypass diode failure [9, 19], potential induced degradation (PID) [9, 45], fragmented glass [14] and light and elevated temperature-induced degradation [14] are identifiable [5]. The PL images were obtained in three studies. The *PL* images in the study on ultranarrow band-pass filters show cracks and isolated regions [38], and those acquired under LED module illumination show PID degradation, cracks and inactive areas [16]. The PL images obtained with laser excitation show cracks and isolated regions. It was shown that the laser's scanning orientation, perpendicular or parallel to busbars, plays an important role as to how an isolated region appears on the PL image in question. Illuminating a line of a cell results in the possibility to detect finger interruptions which are difficult to detect if one illuminates the entire cell area during imaging [28, 46].

Cracks and isolated regions (i.e. areas with increased series resistance) are the type of failure that has been addressed most often. It is important to clarify how isolated regions appear in ΔPL_{OP} (and PCC_{PL} images) compared to PL images. In this context, images obtained under sunlight excitation will be discussed because most data is available from imaging in these conditions. ΔPL_S images are not included in this comparison because there is not enough literature on this subject. EL images are used here as a reference point because they have been used for validation purposes in several studies [5, 18, 21, 23, 34].

5.1. Comparison between EL, ΔPL_{OP} and PCC_{PL} images

Even though ΔPL_{OP} images have been validated with EL_{SC} images, their similarity in terms of pixel intensity depends on the OPs between which the ΔPL_{OP} images are acquired [21, 34]. An example of this is shown in figure 13. An EL_{SC} image of a damaged module, figure 13(a), does not correspond to both ΔPL_{OP} images, figures 13(b) and (c), of the same module. The ΔPL_{OP} images were processed from one data set acquired at different OPs during an IV curve sweep. However, the difference in the extracted current between the OPs in which the images were acquired was the same. Even though the ΔPL_{OP} images correspond to the EL_{SC} image in terms of intensity values in the isolated regions, the image in figure 13(c) differs considerably from the EL_{SC} image with respect to overall signal in the two sub-strings connected in parallel on the left side of the module. This is because the two ΔPL_{OP} images were obtained at different levels of extracted current.

The PCC_{PL} images resulting from the PCC algorithm have shown that they correspond to ΔPL_{OP} images. This correspondence is maintained also in case of different versions of ΔPL_{OP} images, which might result from different levels of current extraction during imaging [22]. This means that PCC_{PL} images also correspond to EL images depending on the OP during which the images were obtained, as explained above.

In order to investigate whether one could process PL images obtained in diffuse irradiance below 100 Wm^{-2} and obtain useful information about module damage, an $EL_{0.1SC}$ image obtained with 10% of SC current, in addition to an EL_{SC}, has been used to validate the PCC_{PL} images obtained in diffuse irradiance [36, 47]. This is shown in figure 14 on the example of the same damaged module as in figure 13. Images simulating and representing high irradiance conditions, figures 14(a) and (b), are shown as comparison to images simulating and representing low irradiance conditions, figures 14(c) and (d).

5.2. Comparison between EL, ΔPL_{OP} and PL images

In order to study a level of isolation of a region due to a crack, it might not be enough to acquire only two ΔPL_{OP} or PCC_{PL} images. Quantification of series resistance of an isolated region relative to an intact region of a module under operation has been studied. The approach is based on obtaining several, in this case five,

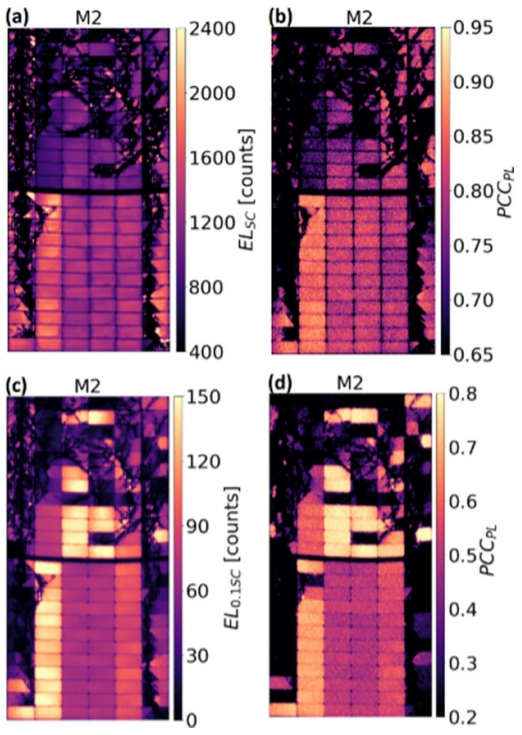

Figure 14. The EL_{SC} image (a), PCC_{PL} image obtained in direct irradiance (b), $EL_{0.1SC}$ image (c) and PCC_{PL} image obtained in diffuse irradiance (d). Reprinted from [36], with the permission of AIP Publishing.

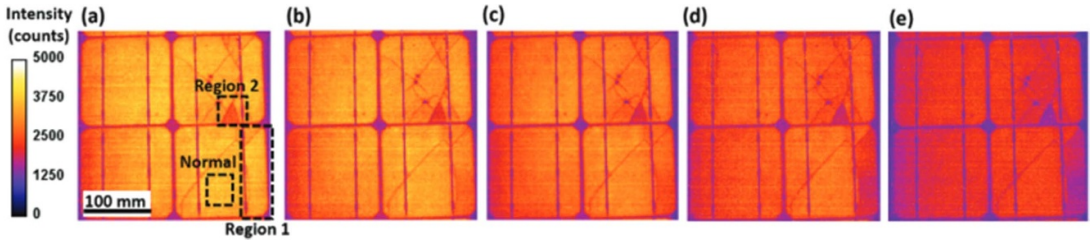

Figure 15. Five ΔPL_{OP} images (a)–(e) are shown of the same module region obtained during five modulation rounds by holding one OP at the OC condition and changing the other along the IV curve. [19] John Wiley & Sons. [© 2019 John Wiley & Sons, Ltd.].

ΔPL_{OP} images from five modulation rounds by holding one OP constant at OC and changing the second OP along the IV curve [19].

Figure 15 shows these images of four cells, where two isolated regions have been emphasized. Region 2 has higher series resistance than Region 1. While Region 2 appears dark on all five ΔPL_{OP} images, Region 1 distinguishes itself from the intact regions of the cell only in the last two images, figures 15(d) and (e). By looking only at figures 15(a) and (b), it is not clear that Region 1 is isolated. In order to get a comprehensive understanding of the isolated regions, two ΔPL_{OP} images, such as those in figures 15(a) and (b), might not suffice. The possibility to distinguish the degree of isolation of a region on a single ΔPL_{OP} image seems, therefore, to depend on the level of current extraction and the degree of isolation of a region.

An example of how PL images appear compared to ΔPL_{OP} images is illustrated in figure 16 with four PL images also obtained at different levels of current extraction. The image in figure 16(a) obtained in OC condition shows cracks, but not the level of isolation of the different regions encircled by the cracks. With the increasing level of current extraction, from figure 16(b) to figure 16(d), the level of isolation becomes apparent. The most isolated region appears the brightest, while the intact regions appear dark. This is exactly the opposite from how the isolated and intact regions appear in ΔPL_{OP} images in figure 15. There, the most isolated region appears the darkest, while the intact region appears the brightest.

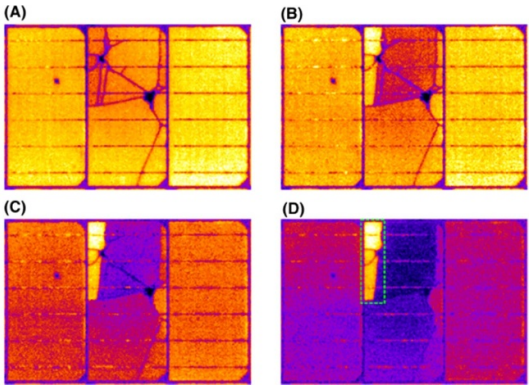

Figure 16. A PL image is obtained in the OC condition (a) while the other three PL images are obtained during current extraction (b)–(d). [38] John Wiley & Sons. [© 2022 The Authors. Progress in Photovoltaics: Research and Applications published by John Wiley & Sons Ltd.

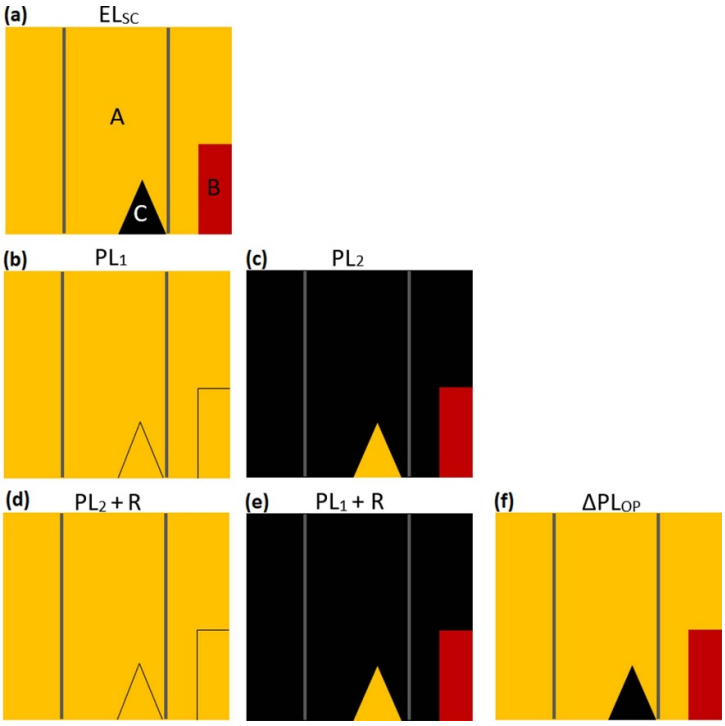

Figure 17. An intact region, A, a partly isolated region, B, and a completely isolated region, C, are shown with the highest, medium and lowest pixel intensity levels in yellow, red and black, respectively, in an EL_{SC} image (a). A PL_1 image obtained in the OC condition (b), a PL_2 image obtained under current extraction, $PL_2 + R$ and $PL_1 + R$ images (d) and (e) obtained under the same conditions as the two preceding images, and a ΔPL_{OP} image (f) obtained after subtraction of $PL_1 + R$ from $PL_2 + R$ [5]. Reproduced with permission from [5]. CC BY-NC-ND 4.0.

The reason for this difference between PL and ΔPL_{OP} images is illustrated in figure 17. An EL_{SC} image in figure 17(a) is used as a point of reference. Three types of regions are shown. Region A is intact, region B is partly isolated and region C is completely isolated. Three colors are used to mark the three levels of pixel intensity in each region. A region of high pixel values is yellow, medium pixel values are red and low pixel values are black, due to the high, medium and low levels of recombination, respectively [5].

If a PL_1 image is obtained in the OC condition, figure 17(b), all three regions will have high-intensity PL signal emission because there is no current extraction in the OC condition. This is visible in figure 16(a) mentioned above. In case of extracted current during acquisition of PL_2, figure 17(c), the completely isolated region C will remain in the OC condition, while the highest level of current density will be extracted from the intact region A because the recombination level in region A is the lowest of the three regions, and it has the

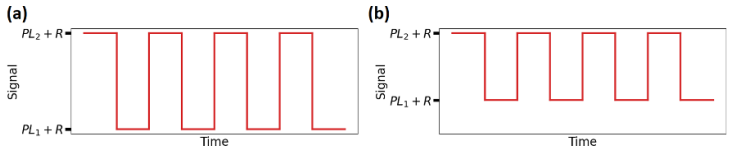

Figure 18. Lock-in approach from figure 5 in which the PL signal is modulated between two levels (a) is used for comparison with modulation when the PL_1 state is set to another point on the IV curve (b). The new PL_1 point is closer to the PL_2 level, meaning that the current levels in (b) are closer to each other than in (a) [5]. Reproduced with permission from [5]. CC BY-NC-ND 4.0.

lowest pixel values. No current is extracted from region C because it is completely isolated from the rest of the cell. Recombination there remains unchanged, and the pixel values remain as high as in the PL_1 image [5].

To obtain a ΔPL_{OP} image, two constituent images are needed, $PL_2 + R$ and $PL_1 + R$, as shown in figures 17(d) and (e). They are acquired under the same conditions as PL_1 and PL_2, and thus, the intensity of the PL signal is the same as in figures 17(b) and (c). However, the reflected solar irradiance values are entailed in $PL_2 + R$ and $PL_1 + R$ on top of the PL signal, and the variation in pixel values in figures 17(d) and (e) is not visible in reality. The ΔPL_{OP} image, figure 17(f), displays pixel values, which are the difference of $PL_2 + R$ and $PL_1 + R$ [5].

How efficiently one can obtain more than two PL, ΔPL_{OP} or PCC_{PL} images, depends on the method for image acquisition presented in section 3. PL imaging during IV curve sweeps is the only approach that, based on one image series, results in several ΔPL_{OP} or PCC_{PL} images [21, 22]. Even though obtaining a PL image with ultranarrow band-pass filters does not require modulation of the OP, the method requires interference with the OP if several PL images are to be acquired. According to the authors, the suitable method for reaching a new OP for another round of imaging is with the optical modulator (several LEDs which manage to change the OP of a string) [38]. In the case of ΔPL_{OP} images, a new round of modulation of the OP is needed to obtain a new ΔPL_{OP} image, as illustrated in figure 18. The original lock-in modulation, as shown in figure 5, is again displayed in figure 18(a) for the sake of comparison with modulation when the PL_1 state is shifted due to another level of current extraction, as shown in figure 18(b). The images acquired during modulation in the latter case will have a smaller ΔPL value due to the smaller current difference between the PL_1 and PL_2 states. The equipment used for modulation of the OP must allow switching between three OPs to obtain two ΔPL_{OP} images. This is the case with the DaySy system [31], MOSFET with a programmable DC load [34], LEDs (optical modulator)[19, 20] and remote switching of the OP through the string inverter [5, 23, 44].

6. Overview

An overview of all the studies on PL imaging approaches and the main aspects that characterize them are shown in table 1. They are the excitation intensity as described or measured in each study, the type of filtering, the filtering equipment used and the PV area size that can potentially be imaged, conditioned by the equipment. Furthermore, the type of modulation applied in case of lock-in technique and its duration is specified as well as what OPs the modulation can be conducted between. A range of OPs is indicated with a hyphen, while discrete OPs are separated by a comma. Finally, the type of PL image that results from each method is specified.

7. Conclusions

Methods and approaches for outdoor PL imaging at night and daytime have been presented. The particular solutions for every approach with respect to filtering of the light from the excitation source has been explained. The approaches for daytime imaging have been divided into three main categories: optical filtering, control of the OP and IV curve sweeps. The differences in acquired and processed images have been explained. Interpretation of different types of processed PL images has been discussed.

The interpretation of PL and ΔPL_{OP} images reported to this date does provide valuable information for localizing and diagnosing of cracks and isolated areas. Severity interpretation is dependable on whether current extraction is available in the detection method or not. As mentioned before, PL is a fairly new approach for fault detection in field-installed PV modules, therefore, the interpretation of a wider range of defects will have to be updated as the technology matures.

Regarding the usefulness of PL imaging for large scale PV inspections, throughput limitation is dependent on the type of filtering equipment utilized. Essentially, all methods work well for PV modules

Table 1. Overview of the main aspects of the different approaches to PL imaging.

Study	Excitation source (Intensity)	Type of filtering	Filtering equipment	PV area	Modulation	Switching duration	OPs	Image type
[16]	18 LEDs ($37\,W\,m^{-2}$)	Optical	Short-pass, long-pass f.	1 module	—	—	—	PL
[17]	4 LEDs ($10–20\,W\,m^{-12}$)	Optical	Short-pass, long-pass f.	1 module	—	—	—	PL
[28]	Laser (3.2 Suns)	Optical	Long-pass f.	1 module	—	—	—	PL
[38]	Sun (full sunlight)	Optical	Ultranarrow band-pass f.	>1 string	—	—	—	PL
[37]	Sun (full sunlight)	Optical	Two band-pass f.	>1 string	—	—	—	ΔPL_S
[31–33]	Sun ($>80\,W\,m^{-2}$)	Lock-in	DaySyBox	6 strings	electrical	I[a]	SC, MPP, OC	ΔPL_{OP}
[34]	Sun	Lock-in	MOSFET+DC load	1 module	electrical	I	SC-OC	ΔPL_{OP}
[12]	Sun ($>260\,W\,m^{-2}$)	Lock-in	Solid-state relay	1 module	electrical	I	SC, OC	ΔPL_{OP}
[35]	Sun (clear sky)	Lock-in	String inverter, combiner box	>1 string	electrical	D	MPP, OC	ΔPL_{OP}
[23, 44]	Sun(full sunlight)	Lock-in	String inverter	>1 string	electrical	D	MPP-OC	ΔPL_{OP}
[18]	Sun (full sunlight)	Lock-in	LED	1 sub-string	optical	I	SC-OC	ΔPL_{OP}
[19]	Sun (full sunlight)	Lock-in	LED + microinverter	1 module	optical	D	MPP-OC	ΔPL_{OP}
[20]	Sun (full sunlight)	Lock-in	Optical modulator	1 string	optical	I	MPP-OC	ΔPL_{OP}
[21]	Sun ($\approx 800\,W\,m^{-2}$)	IV curve sweep	String inverter	>1 string	—	—	—	ΔPL_{OP}
[22]	Sun ($\approx 800\,W\,m^{-2}$)	IV curve sweep	String inverter	>1 string	—	—	—	PCC_{PL}
[36]	Sun ($<100\,W\,m^{-2}$)	IV curve sweep	String inverter	>1 string	—	—	—	PCC_{PL}

[a] I: Instantaneous, D: Delayed

with state-of-the-art solar cell technologies with high V_{OC}. However, that might not be the case for old installations containing modules with lower V_{OC}, i.e. Al-BSF modules.

Data availability statement

No new data were created or analysed in this study.

Acknowledgments

This work was performed within The Norwegian Research Center for Sustainable Solar Cell Technology (FME SUSOLTECH, Project Number 257639/E20). The center is co sponsored by the Research Council of Norway and its research and industry partners.

ORCID iD

M Vuković https://orcid.org/0000-0003-1148-5958

References

[1] Kenny R 2024 1 TW and counting (available at: www.eupvsec.org/images/2023/news/eupvsec2023_NewsNo1/EUPVSEC2023-NewsNo1.html) (Accessed 15 February 2024)
[2] Bahar H 2022 Renewables 2022: analysis and forecast to 2027 *Technical Report* International Energy Agency
[3] Meribout M, Tiwari V K, Herrera J P P and Baobaid A N M A 2023 Solar panel inspection techniques and prospects *Measurement* **209** 112466
[4] Meribout M 2023 Sensor systems for solar plant monitoring *IEEE Trans. Instrum. Meas.* **72** 1–16
[5] Vuković M 2023 Toward monitoring of photovoltaic power plants with photoluminescence imaging *PhD Thesis* Norwegian University of Life Sciences
[6] Høiaas I, Grujic K, Imenes A G, Burud I, Olsen E and Belbachir N 2022 Inspection and condition monitoring of large-scale photovoltaic power plants: a review of imaging technologies *Renew. Sustain. Energy Rev.* **161** 112353
[7] Waqar Akram M, Li G, Jin Y and Chen X 2022 Failures of photovoltaic modules and their detection: a review *Appl. Energy* **313** 118822
[8] Kunz O, Schlipf J, Fladung A, Khoo Y S, Bedrich K, Trupke T and Hameiri Z 2022 Outdoor luminescence imaging of field-deployed PV modules *Prog. Energy* **4** 042014
[9] Herrmann W *et al* 2021 Qualification of photovoltaic PV power plants using mobile test equipment *IEA-PVPS* T13-24: 2021
[10] Grimaccia F, Leva S, Dolara A and Aghaei M 2017 Survey on PV modules' common faults after an O&M flight extensive campaign over different plants in Italy *IEEE J. Photovolt.* **7** 810–6
[11] Köntges M, Morlier A, Eder G, Fleiß E, Kubicek B and Lin J 2020 Review: Ultraviolet fluorescence as assessment tool for photovoltaic modules *IEEE J. Photovolt.* **10** 616–33
[12] Guada M, Moretón A, Rodriguez-Conde S, Sánchez L A, Martinez M, González M A, Jiménez J, Pérez L, Parra V and Martinez O 2020 Daylight luminescence system for silicon solar panels based on a bias switching method *Energy Sci. Eng.* **8** 3839–53
[13] Kropp T, Berner M, Stoicescu L and Werner J H 2017 Self-sourced daylight electroluminescence from photovoltaic modules *IEEE J. Photovolt.* **7** 1184–9
[14] Koester L, Lindig S, Louwen A, Astigarraga A, Manzolini G and Moser D 2022 Review of photovoltaic module degradation, field inspection techniques and techno-economic assessment *Renew. Sustain. Energy Rev.* **165** 112616
[15] Trupke T, Mitchell B, Weber J, McMillan W, Bardos R and Kroeze R 2012 Photoluminescence imaging for photovoltaic applications *Energy Proc.* **15** 135–46
[16] Doll B, Hepp J, Hoffmann M, Schüler R, Buerhop-Lutz C, Peters I M, Hauch J A, Maier A and Brabec C J 2021 Photoluminescence for defect detection on full-sized photovoltaic modules *IEEE J. Photovolt.* **11** 1419–29
[17] Doll B, Wittmann E, Lüer L, Hepp J, Buerhop-Lutz C, Hauch J A, Brabec C J and Peters I M 2023 Aerial photoluminescence imaging of photovoltaic modules *Physica Status Solidi (RRL)* **17** 2300059
[18] Bhoopathy R, Kunz O, Juhl M, Trupke T and Hameiri Z 2018 Outdoor photoluminescence imaging of photovoltaic modules with sunlight excitation *Prog. Photovolt., Res. Appl.* **26** 69–73
[19] Bhoopathy R, Kunz O, Juhl M, Trupke T and Hameiri Z 2020 Outdoor photoluminescence imaging of solar panels by contactless switching: technical considerations and applications *Prog. Photovolt., Res. Appl.* **28** 217–28
[20] Kunz O, Rey G, Juhl M K and Trupke T 2021 High throughput outdoor photoluminescence imaging via PV string modulation *IEEE 48th Photovoltaic Specialists Conf. (PVSC)* (IEEE) pp 0346–50
[21] Vuković M, Jakovljević M, Flø A S, Olsen E and Burud I 2022 Noninvasive photoluminescence imaging of silicon PV modules in daylight *Appl. Phys. Lett.* **120** 244102
[22] Vuković M, Liland K H, Indahl U, Jakovljević M, Flø A S, Olsen E and Burud I 2023 Extraction of photoluminescence with pearson correlation coefficient from images of field-installed photovoltaic modules *J. Appl. Phys.* **133** 214901
[23] Vuković M, Høiaas I E, Jakovljević M, Flø A S, Olsen E and Burud I 2022 Photoluminescence imaging of silicon modules in a string *Prog. Photovolt., Res. Appl.* **30** 436–46
[24] Burud I, Mehl T, Flo A, Lausch D and Olsen E 2016 Hyperspectral photoluminescence imaging of defects in solar cells *J. Spectral Imaging* **5** 1–5
[25] Photonics R 2024 Owl 1280 (available at: www.raptorphotonics.com/products/owl-1280/) (Accessed 15 February 2024)
[26] Doll B, Hoffmann M, Stroyuk O and Vetter A 2020 Contactless outdoor photoluminescence of silicon photovoltaic modules with large area excitation source *Proc. 37th Eur. Photovolt. Sol. Energy Conf. Exhib.* pp 1370–3
[27] NREL 2023 A faster, cheaper way to give solar panels a clean bill of health (available at: www.nrel.gov/news/program/2023/a-faster-cheaper-way-to-give-solar-panels-a-clean-bill-of-health.html) (Accessed 20 September 2023)

[28] dos Reis Benatto G A, Lancia A A S, Hass T K, Poulsen P B and Spataru S 2020 Detection of solar cell cracks by laser line induced lateral currents and luminescence imaging *37th European Photovoltaic Solar Energy Conf. and Exhibition* pp 1053–7
[29] Mantel C, dos Reis Benatto G A, Lancia A A S, Spataru S, Poulsen P B and Forchhammer S 2022 Reconstruction and calibration of contactless electroluminescence images from laser line scanning of photovoltaic modules *IEEE J. Photovolt.* **12** 696–702
[30] Honsberg C B and Bowden S G 2019 Photovoltaics education website (available at: www.pveducation.org) (Accessed 12 May 2023)
[31] Stoicescu L, Reuter M and Werner J H 2014 Daysy: luminescence imaging of PV modules in daylight *29th European Photovoltaic Solar Energy Conf. and Exhibition* pp 2553–4
[32] Stoicescu L, Reutner M and Werner J H 2015 Method and apparatus for testing photovoltaic modules *United States Patent US* 9,680,412 B2
[33] GMBH S S 2019 Daysy - daylight luminescence system - measurement guide (available at: www.solarzentrum-stuttgart.com/uploads/file/DaySy_Measurement_Guide_current.pdf) (Accessed 01 April 2023)
[34] Silverman T J, Deceglie M G, VanSant K, Johnston S and Repins I 2017 Illuminated outdoor luminescence imaging of photovoltaic modules *IEEE 44th Photovoltaic Specialist Conf. (PVSC)* (IEEE) pp 3452–5
[35] Koester L, Astigarraga A, Lindig S, Louwen A, Antinori M, Moser D and Manzolini G 2021 Quality assurance of the photovoltaic power plants installation stage-a complementary strategy based of photoluminescence and steady-state thermography *Proc. 38th European Photovoltaic Solar Energy Conf. and Exhibition* pp 1042–50
[36] Vuković M, Hillestad M, Jakovljević M, Flø A S, Olsen E and Burud I 2023 Photoluminescence imaging of field-installed photovoltaic modules under diffuse irradiance *J. Appl. Phys.* **134** 074903
[37] Kunz O, Rey G, Bhoopathy R, Hameiri Z and Trupke T 2020 Outdoor PL imaging of crystalline silicon modules at constant operating point *47th IEEE Photovoltaic Specialists Conf. (PVSC)* (IEEE) pp 2140–3
[38] Rey G, Kunz O, Green M and Trupke T 2022 Luminescence imaging of solar modules in full sunlight using ultranarrow bandpass filters *Prog. Photovolt., Res. Appl.* **30** 1115–21
[39] Breitenstein O, Warta W and Langenkamp M 2010 *Lock-in Thermography: Basics and Use for Evaluating Electronic Devices and Materials* vol 10 (Springer)
[40] Fronius I (GmbH) 2022 Lower losses in the case of partial shading of pv systems (available at: www.fronius.com/en/solar-energy/installers-partners/products-solutions/features/dynamic-peak-manager) (Accessed 8 May 2023)
[41] C. G. C. Center and L. Huawei Technologies Co. 2020 Smart I-V curve diagnosis: technical white paper (available at: https://solar.huawei.com/en-GB/download?p=%2F-%2Fmedia%2FSolar%2Fnews%2Fwhitepaper%2FIV-Curve-whitepaper.pdf) (Accessed 8 May 2023)
[42] Danfoss 2010 Tlx reference manual (available at: www.technosun.com/descargas/DANFOSS-TLX6-TLX8-TLX10-TLX12.5-TLX15kW-manual-referencia-EN.pdf) (Accessed 8 May 2023)
[43] Sungrow 2020 Data-driven monitoring starts at the inverter (available at: https://16iwyl195vvfgoqu3136p2ly-wpengine.netdna-ssl.com/wp-content/uploads/2020/07/02-pv-magazine-Webinar_Presentation-of-Sungrow_July-28th.pdf) (Accessed 8 May 2023)
[44] Vuković M, Høiaas I E, Jakovljević M, Flø A S, Olsen E and Burud I 2022 Outdoor photoluminescence and electroluminescence imaging of photovoltaic silicon modules in a string *AIP Conf. Proc.* **2487** 030012
[45] Stoicescu L and Reuter M 2018 Daysy contactless measurements of PID shunt resistance in installed PV modules *25th European Photovoltaic Solar Energy Conf. and Exhibition* pp 1337–9
[46] Zafirovska I, Juhl M K, Weber J W, Wong J and Trupke T 2017 Detection of finger interruptions in silicon solar cells using line scan photoluminescence imaging *IEEE J. Photovolt.* **7** 1496–502
[47] Mühleisen W *et al* 2019 Scientific and economic comparison of outdoor characterisation methods for photovoltaic power plants *Renew. Energy* **134** 321–9